Supporting information

The Volcano Trend in Electrocatalytic CO_2 Reduction Activity over Atomically-Dispersed Metal Sites on Nitrogen-Doped Carbon

*Jingkun Li[1], Paulina Pršlja[2], Tatsuya Shinagawa[3], Antonio José Martín Fernández[3], Frank Krumeich[4], Kateryna Artyushkova[5], Plamen Atanassov[6], Andrea Zitolo[7], Yecheng Zhou[2], Rodrigo García-Muelas[2], Núria López[2], Javier Pérez-Ramírez[3], and Frédéric Jaouen[1]**

1 Institut Charles Gerhardt Montpellier, UMR 5253, CNRS, Université Montpellier, ENSCM, Place Eugène Bataillon, 34095 Montpellier cedex 5, France

2 Institute of Chemical Research of Catalonia, ICIQ, The Barcelona Institute of Science and Technology, Av. Països Catalans, 16, 43007 Tarragona, Spain

3 Institute for Chemical and Bioengineering, Department of Chemistry and Applied Biosciences, ETH Zurich, Vladimir-Prelog-Weg 1, 8093 Zurich, Switzerland

4 Laboratory of Inorganic Chemistry. Department of Materials, ETH Zurich, Vladimir-Prelog-Weg 1, 8093 Zurich, Switzerland

5 The Department of Chemical and Biological Engineering, Center for Micro-Engineered Materials (CMEM), University of New Mexico, Albuquerque, NM 87131, USA

6 Chemical and biomolecular engineering, University of California Irvine, Irvine, CA 92697, USA

7 Synchrotron SOLEIL, L'Orme des Merisiers, BP 48 Saint Aubin, 91192 Gif-sur-Yvette, France

Corresponding author: frederic.jaouen@umontpellier.fr

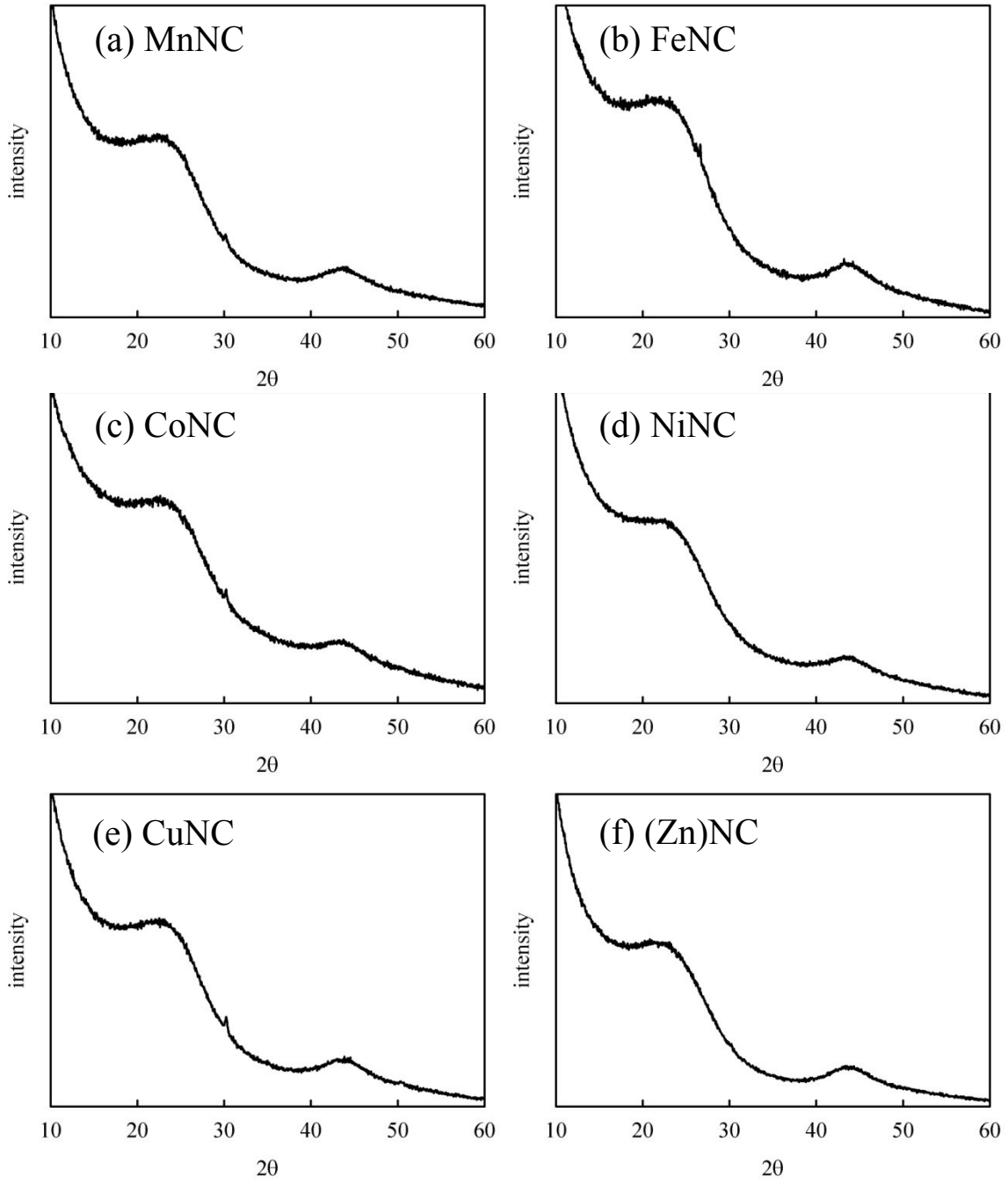

Figure S1. XRD patterns of (a) MnNC, (b) FeNC, (c) CoNC, (d) NiNC, (e) CuNC, and (f) (Zn)NC.

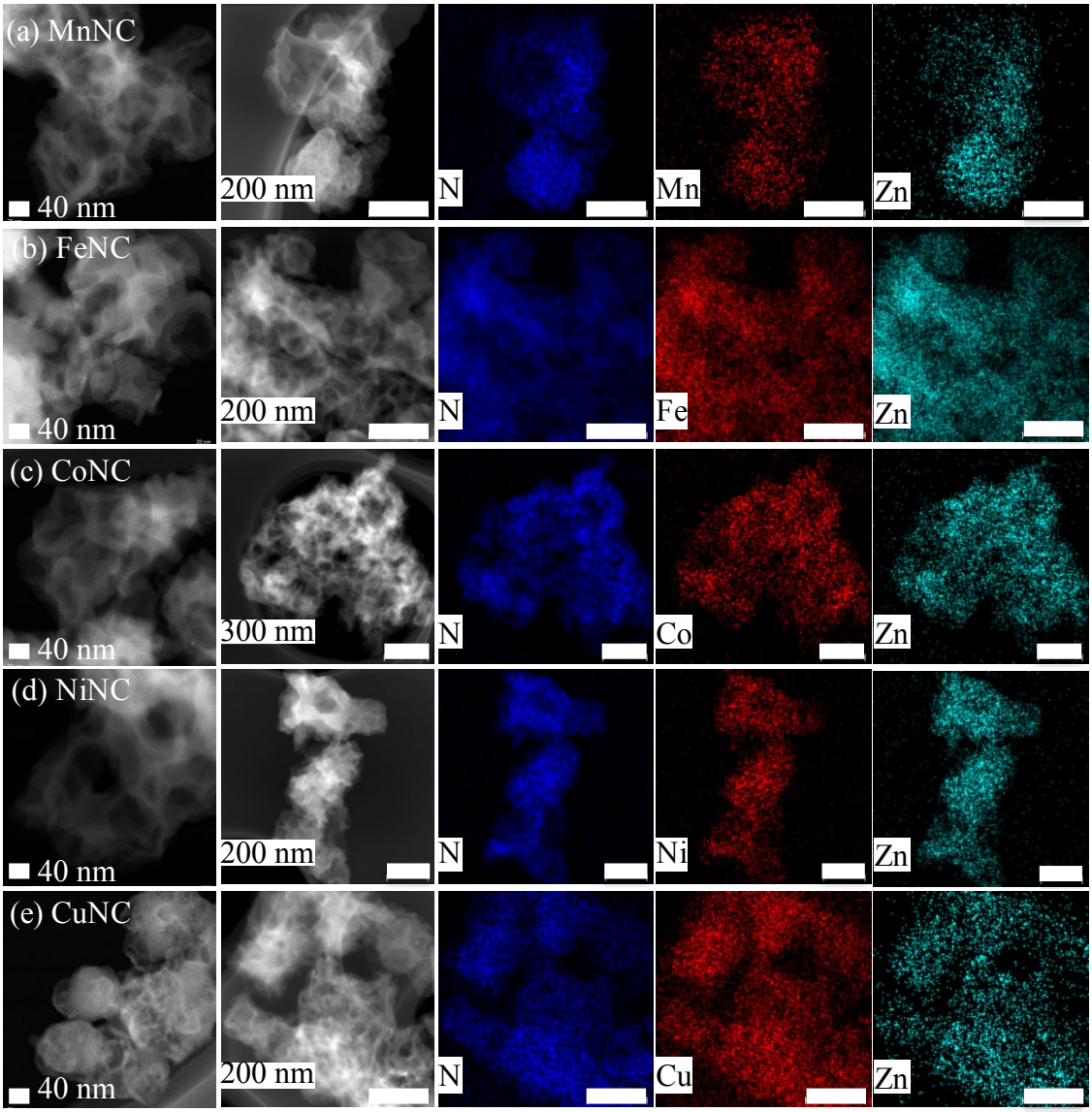

Figure S2. (S)TEM images and EDX elemental mapping for C, N, Zn and the respective metal derived from the metal-acetate precursor of (a) MnNC, (b) FeNC, (c) CoNC, (d) NiNC and (e) CuNC.

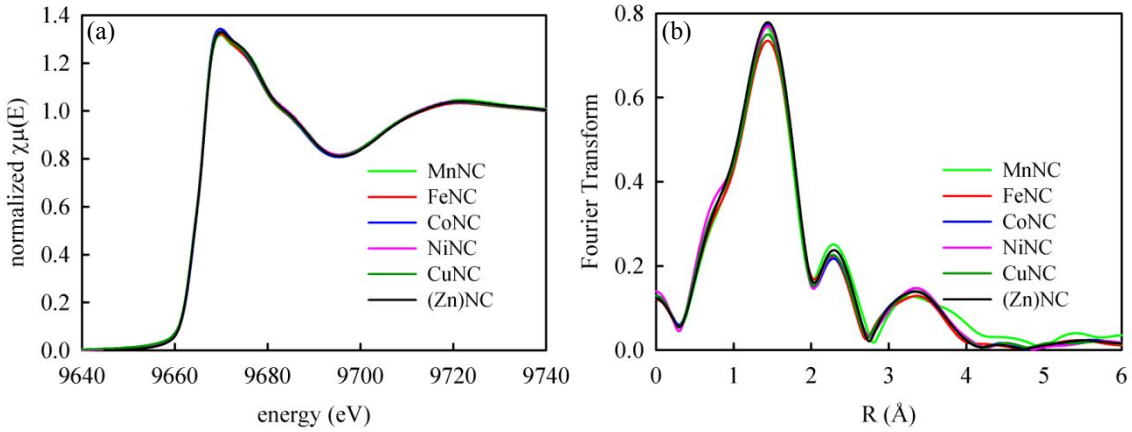

Figure S3. (a) Zn K-edge XANES spectra, and (b) the corresponding Zn K-edge FT-EXAFS spectra of MNC catalysts.

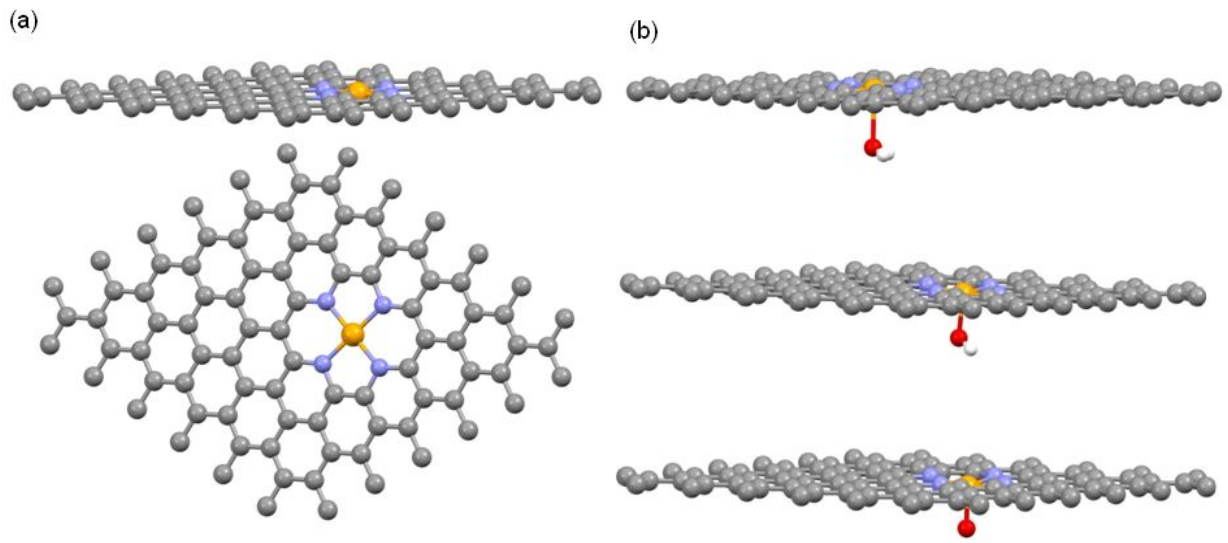

Figure S4. Computational models for the atomically-dispersed MN_4 sites. (a) side and top views (b) when axial ligand is present (L = H_2O, OH, O). C is represented by grey spheres, N by blue, the metal in yellow, O in red and H in white.

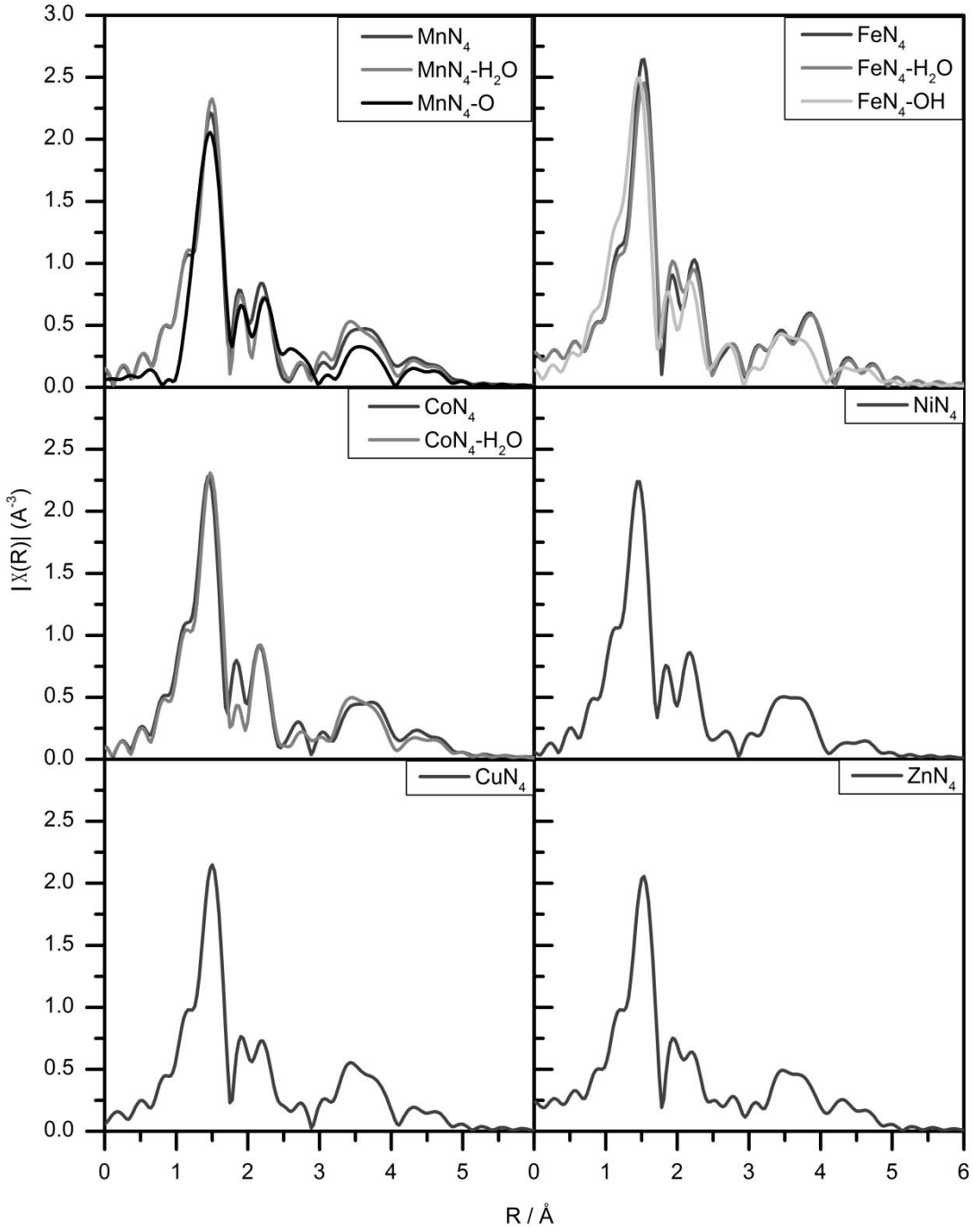

Figure S5. Simulated metal K-edge EXAFS. (a) MnNC, (b) FeNC, (c) CoNC, (d) NiNC, (e) CuNC, and (f) (Zn)NC. For Mn, Fe, and Co all the relevant computed structures are presented.

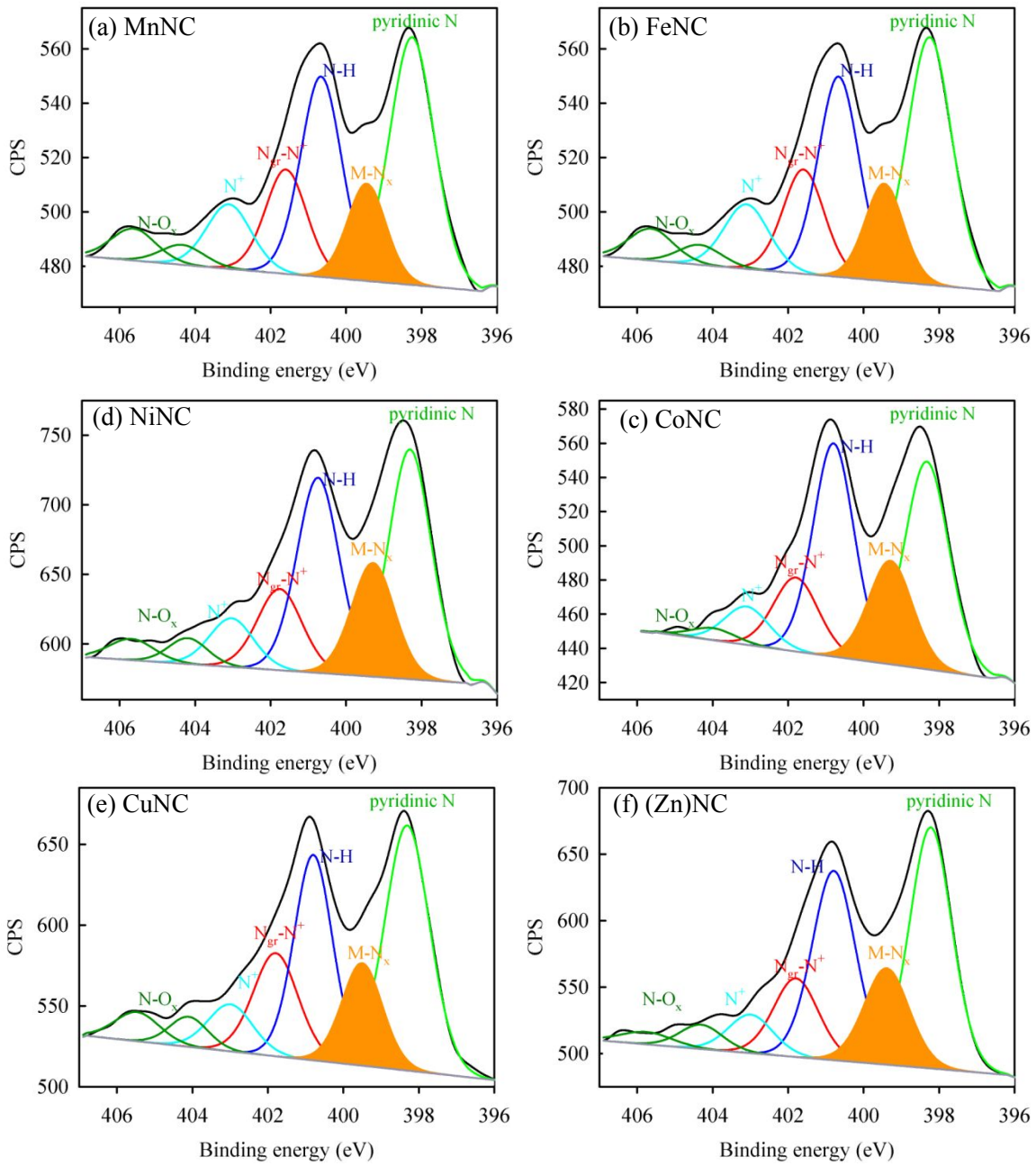

Figure S6. N_{1s} spectra of (a) MnNC, (b) FeNC, (c) CoNC, (d) NiNC, (e) CuNC, and (f) (Zn)NC.

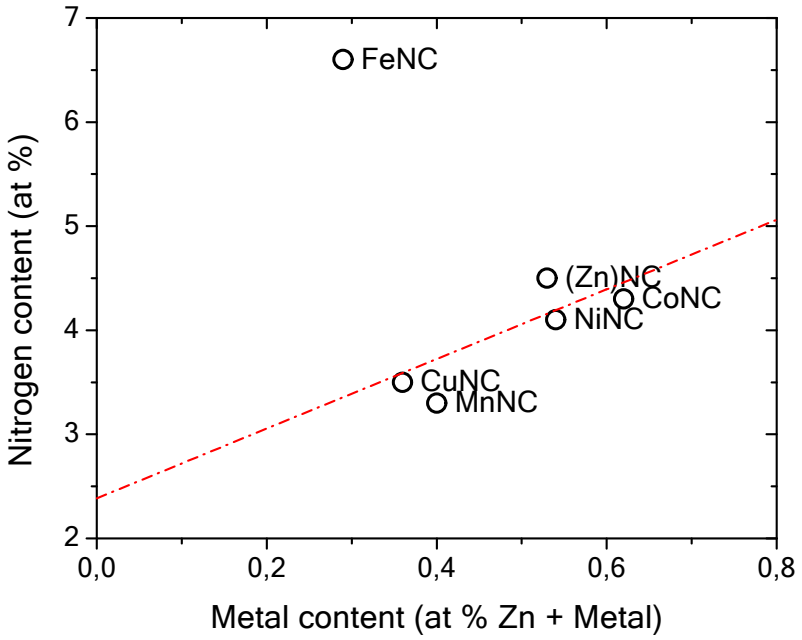

Figure S7. Positive correlation between nitrogen content measured by XPS and the total amount of metal present in the sample (sum of Zn and M). The red line is the fitting obtained considering (Zn)NC, CoNC, NiNC and CuNC. The fitted parameters of the red line are a y-intercept of 2.38 at 0 metal content and a slope of 3.34.

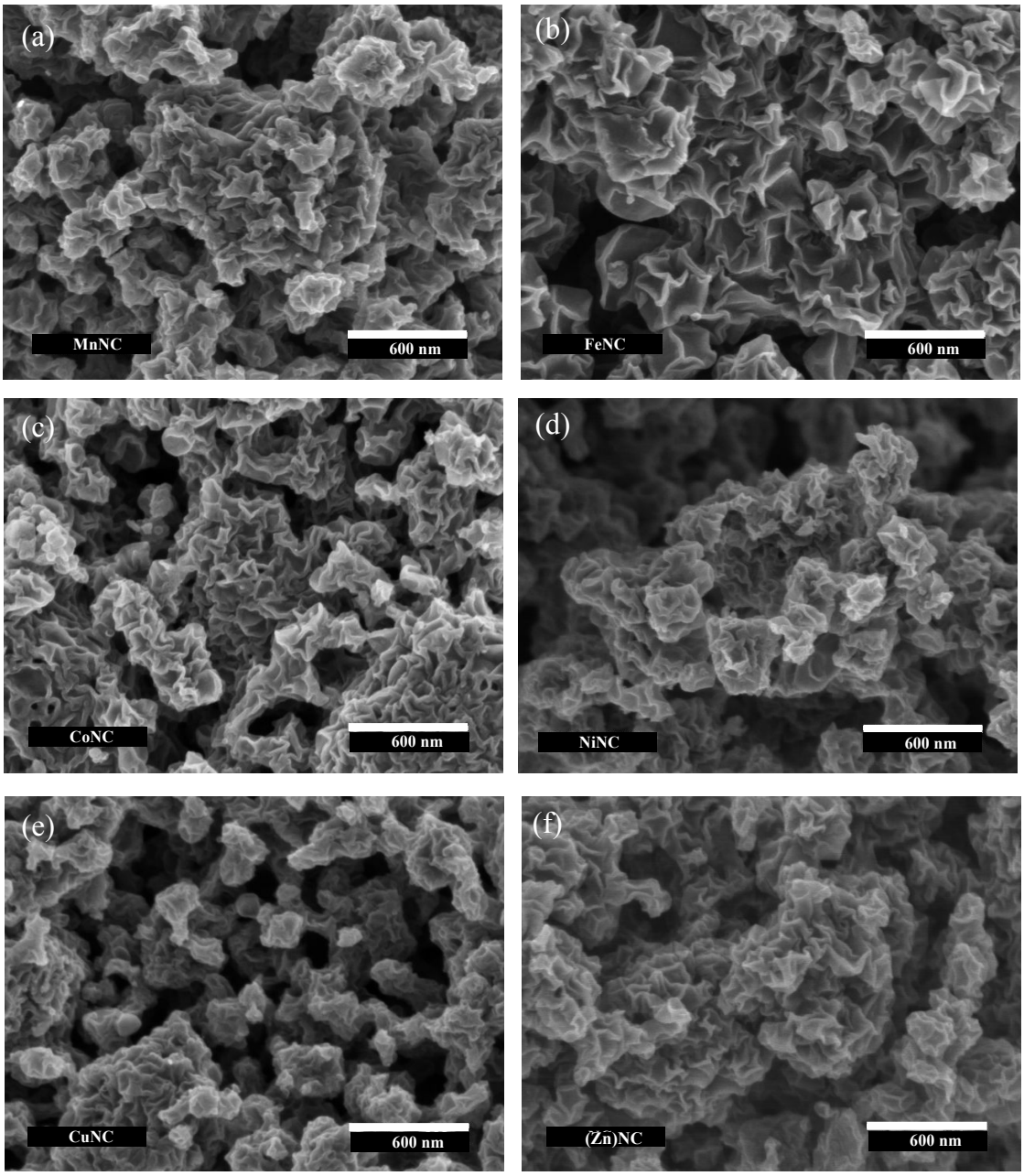

Figure S8. SEM images of (a) MnNC, (b) FeNC, (c) CoNC, (d) NiNC, (e) CuNC, and (f) (Zn)NC.

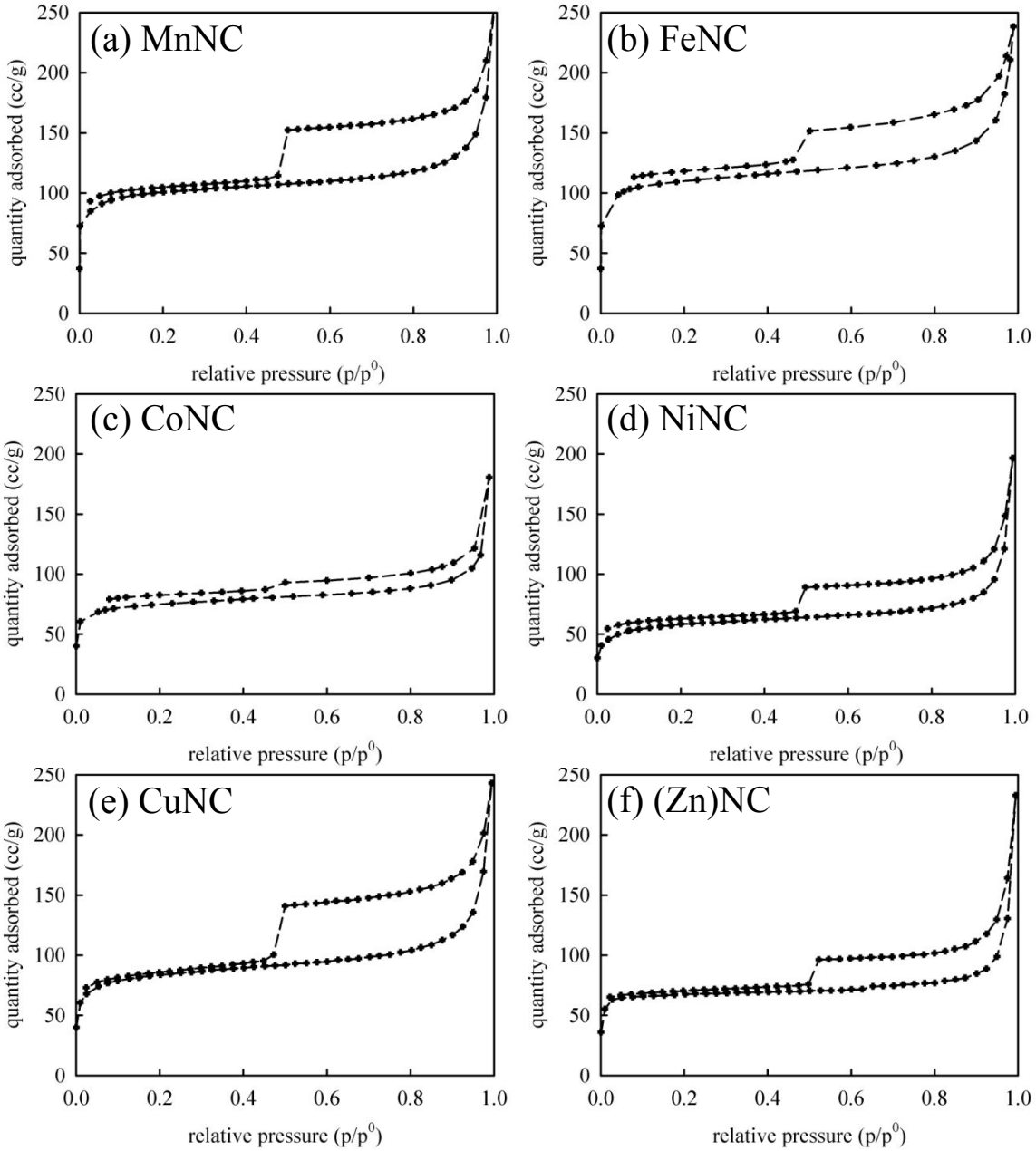

Figure S9. (a) N_2 physisorption isotherms of (a) MnNC, (b) FeNC, (c) CoNC, (d) NiNC, (e) CuNC, and (f) (Zn)NC.

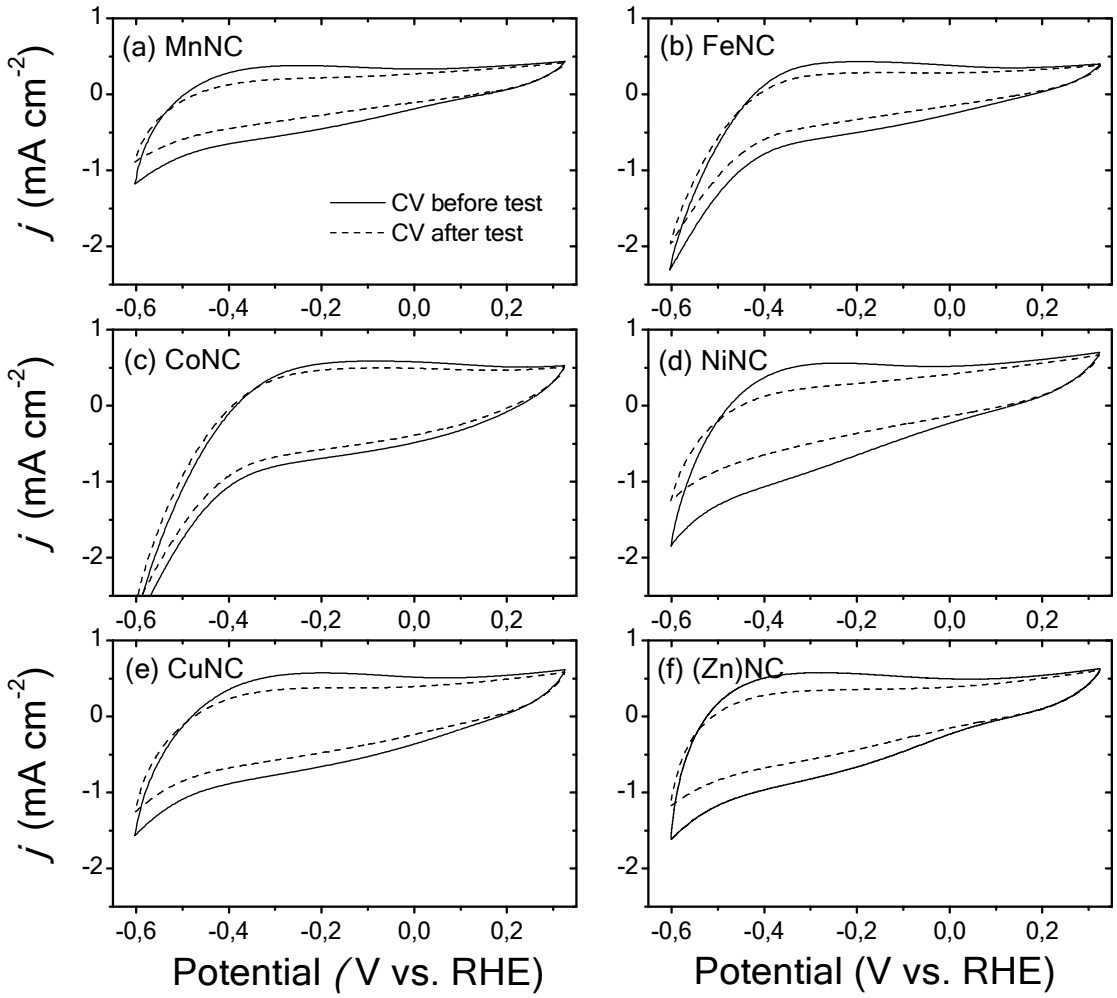

Figure S10. Cyclic voltammograms over (a) MnNC, (b) FeNC, (c) CoNC, (d) NiNC, (e) CuNC, and (f) (Zn)NC, performed in 0.1 M $KHCO_3$ saturated with CO_2 (pH 6.7) at room temperature.

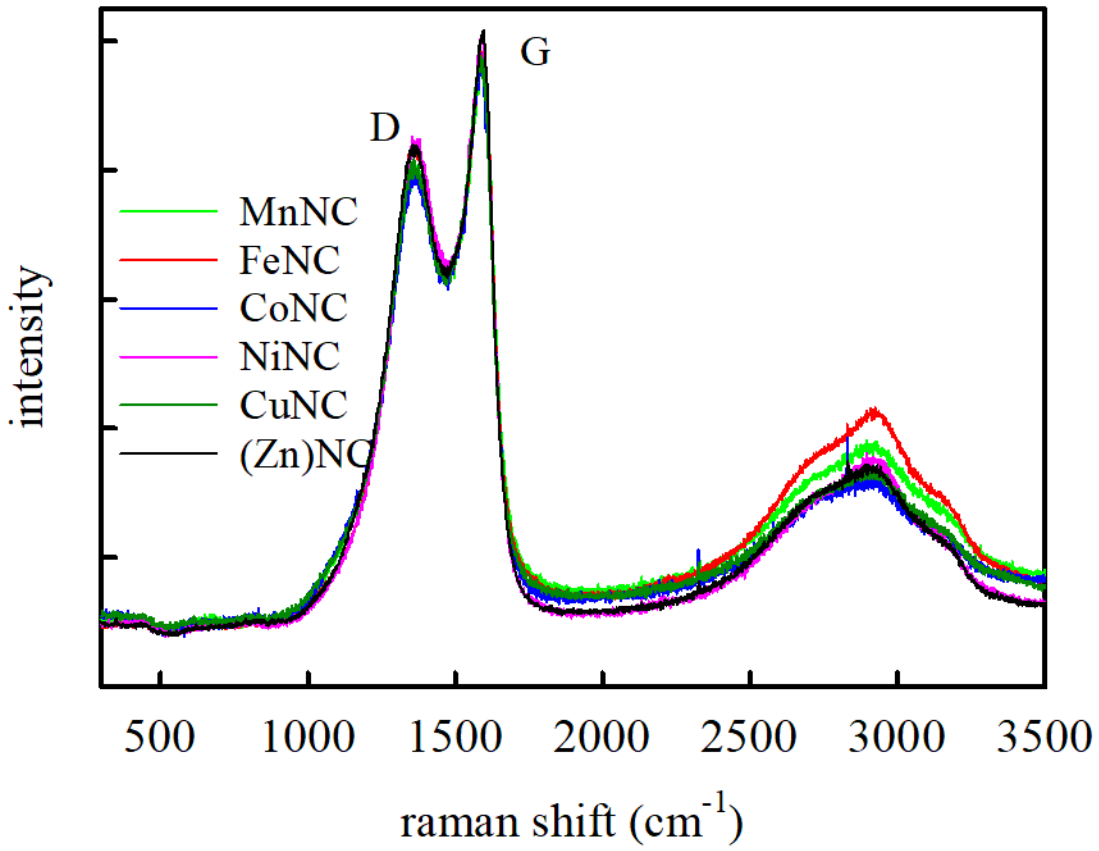

Figure S11. Raman spectra of MNC catalysts.

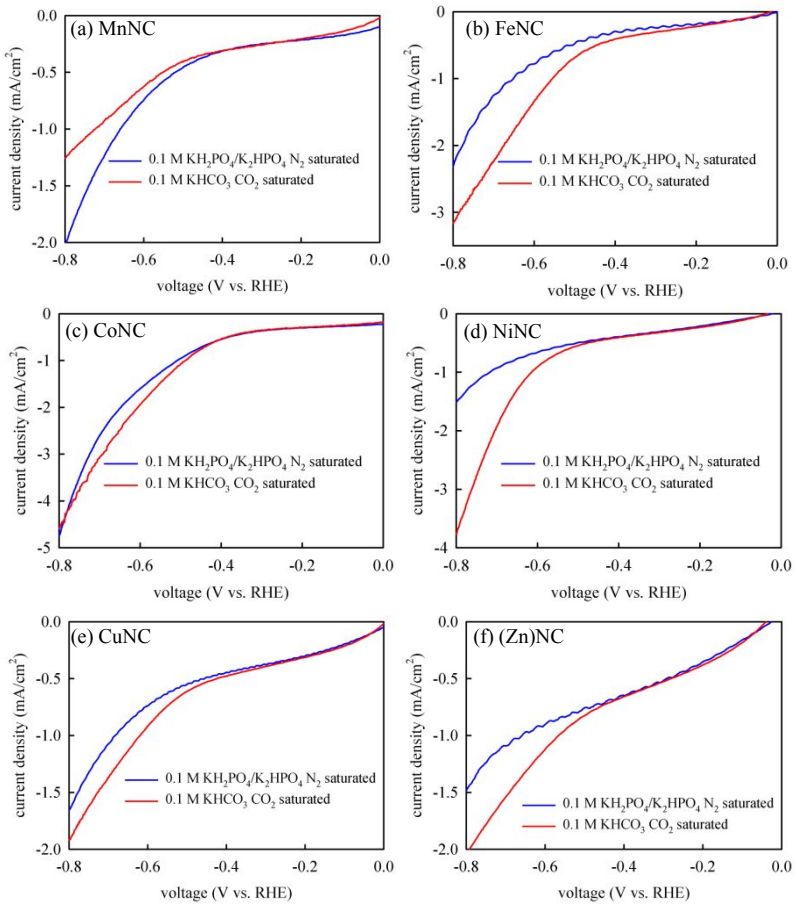

Figure S12. LSV of (a) MnNC, (b) FeNC, (c) CoNC, (d) NiNC, (e) CuNC and (f) (Zn)NC in CO_2-saturated 0.1 M $KHCO_3$ (red curves) and N_2-saturated 0.1 M KH_2PO_4/K_2HPO_4 (blue curves). The catalyst loading is 0.8 mg·cm^{-2} and scan rate is 5·mV s^{-1} in the cathodic direction. Note that the total reduction current on MnNC is higher in the absence of CO_2 (blue vs. red line in Figure S12a) and there might be two possible reasons for this: 1) The presence of CO_2 reduces the HER on MnNC, resulting in a lower total current in the presence of CO_2. 2) Since a KH_2PO_3/K_2HPO_3 buffer is used as a CO_2-free electrolyte to keep a constant pH in the absence of CO_2 (while $KHCO_3$ electrolyte was used in presence of CO_2), it is possible that the HER activity of MnNC is influenced by anions in the electrolytes more than other metals, resulting in a higher HER current in the phosphate buffer electrolyte.

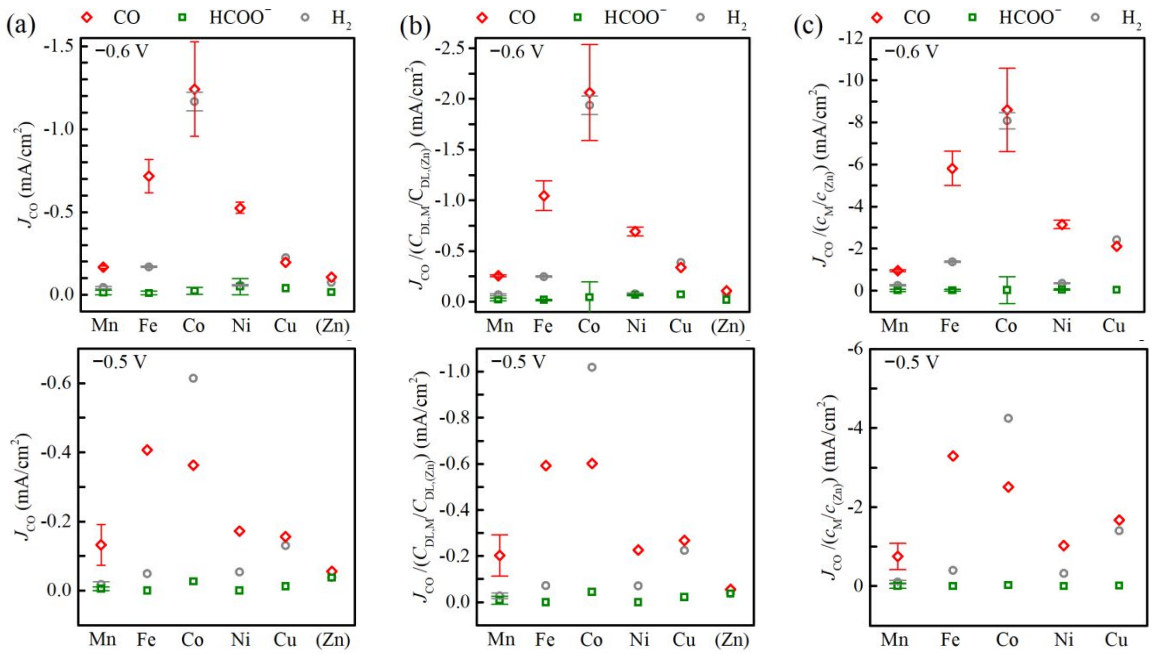

Figure S13. Volcano plots for partial current densities for CO (a), volcano plots after normalization by the relative double layer capacitance (b), and volcano plots after normalization by the relative metal content (c). To calculate the relative capacitance and metal contents, we took (Zn)NC as reference point. For (b), the CO partial current density normalized by the relative double layer capacitance was calculated according to the following equation: $Y\ axis = \frac{J_{CO}}{C_{DL,M}/C_{DL,(Zn)}}$, where $C_{DL,M}$ (μF·cm^{-2}) is the double layer capacitance of MNC measured after testing and $C_{DL,Zn}$ is the double layer capacitance of (Zn)NC measured after testing. For (c), the CO partial current density normalized by the relative metal content was calculated according to the following equation: $Y\ axis = \frac{J_{CO}}{c_M/c_{(Zn)}}$, where c_M is the metal content of interest in MNC (at%) measured by XPS, and $c_{(Zn)}$ the Zn metal content in (Zn)NC.

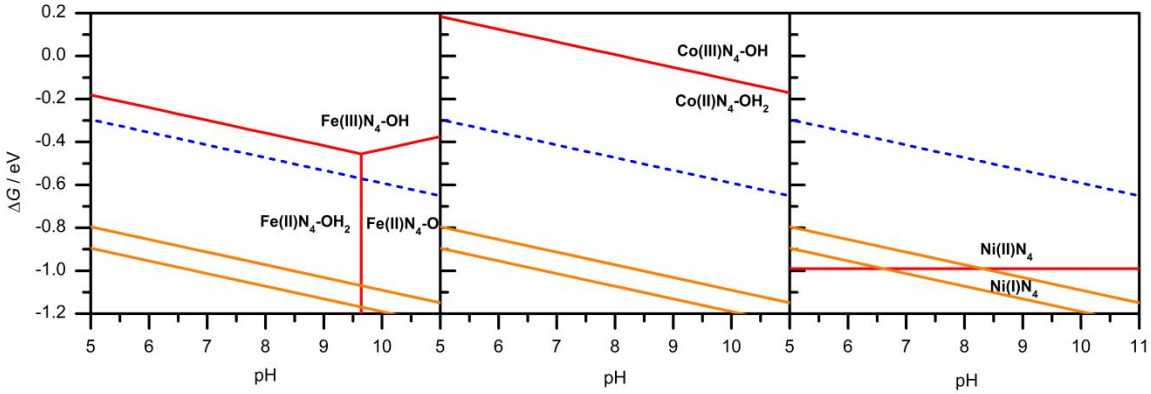

Figure S14. Simulated Pourbaix diagrams. Computed Pourbaix diagram for Fe, Co and Ni in the nitrogen cavities of C. The blue lines corresponding to the water oxidation reactions, the red lines separate the different phases, and the area between two orange lines corresponds to the experimental potential window at which eCO_2RR was evaluated (−0.5 and −0.6 V *vs.* RHE).

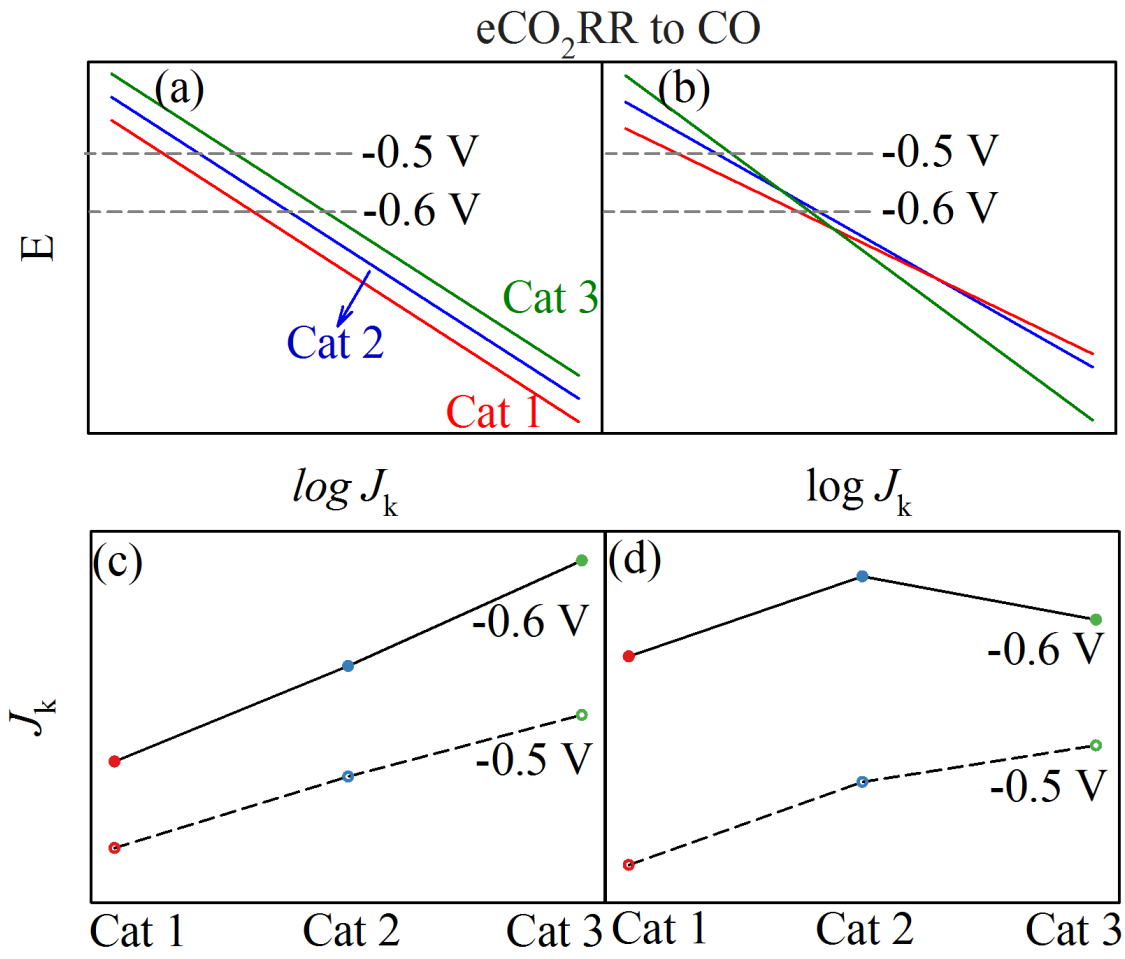

Figure S15. Calculated electrochemical potential *vs*. logarithm of the reaction rate of eCO_2RR to CO assuming (a) a same Tafel slope (60 mV·dec^{-1} for all three catalysts) and (b) different Tafel slopes (50, 60 and 70 mV·dec^{-1} for Cat 1 (red), Cat 2 (blue) and Cat 3 (green), respectively), and (c), (d) the corresponding activity trend at −0.5 and −0.6 V *vs*. RHE derived from the reaction rates in (a) and (b), respectively. The exchange current densities (i_0, values normalized by the lowest one) for Cat 1, Cat 2 and Cat 3 were assumed to be 1, 2 and 4, respectively.

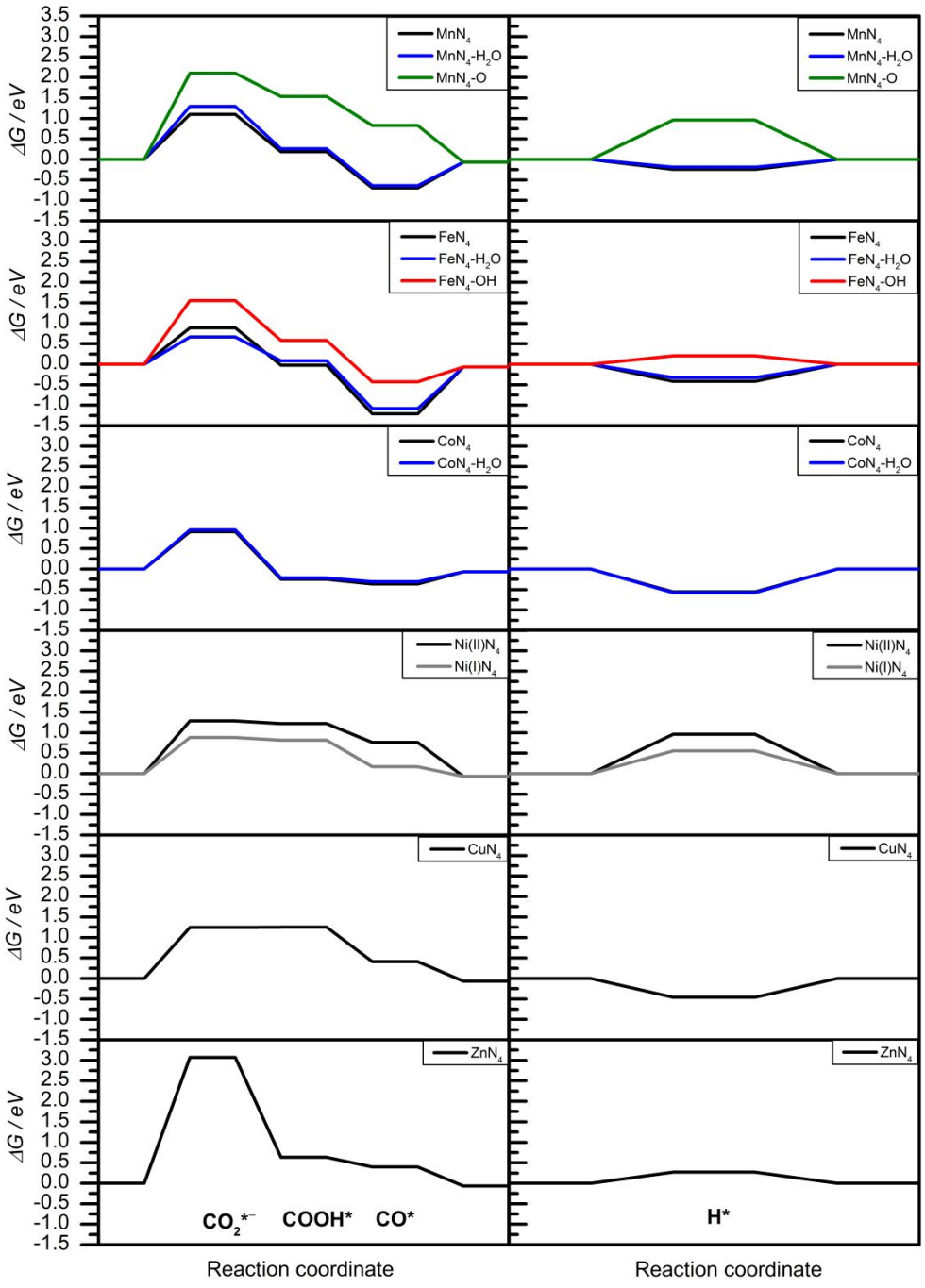

Figure S16. Gibbs free energy profiles of eCO_2RR (left side) and HER (right side) over MN_4C_{10} model sites (M = Mn, Fe, Co, Ni, Cu and Zn) at pH = 7 and U = 0.0 V *vs.* RHE, according to the different metal speciation.

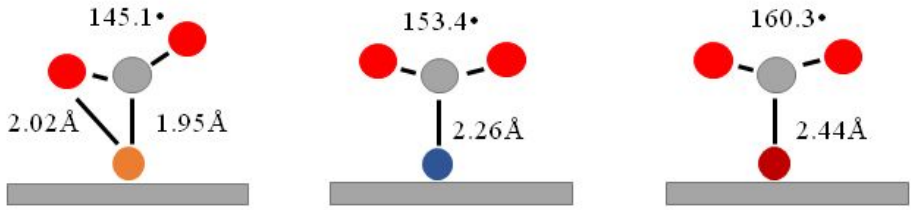

Figure S17. Schematic representation of CO_2 coordination to Fe(II)N_4(-H_2O), Co(II)N_4(-H_2O) and Ni(I)N_4, in the order from the left to the right. While Fe presents an η^2-C,O hapticity with an Fe-O contact, this is absent for Co or Ni that prefer the η^1-C configuration. The CO_2 activation correlates with the difference between the O-C-O bond angle after (angle indicated in scheme above) and before (180°) its adsorption on the metal cation, that increases from *ca* 20º to 35° along the Ni, Co, Fe series.

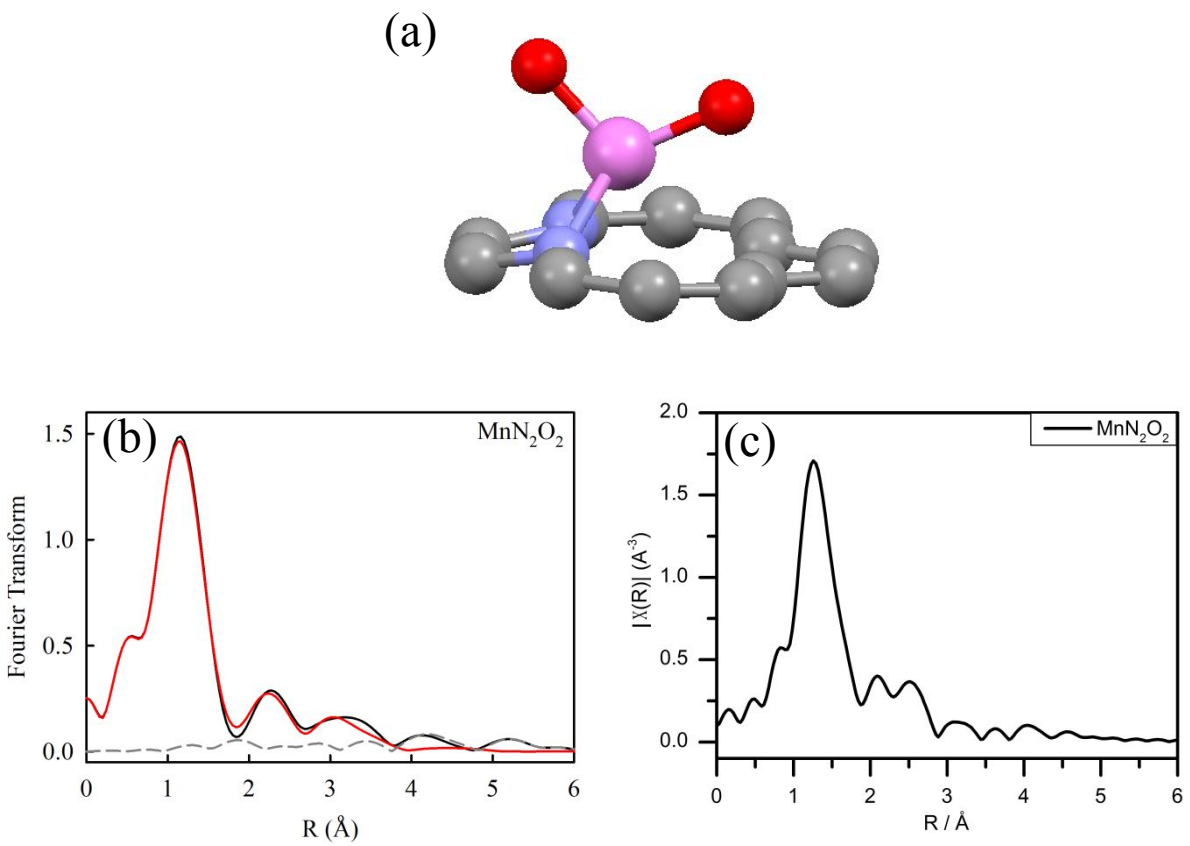

Figure S18. (a) Computational model for MnN_2O_2 site. (b) Mn K-edge EXAFS spectrum of MnNC fitted with MnN_2O_2 structure. (c) DFT simulated metal K-edge EXAFS spectrum of MnN_2O_2 model site.

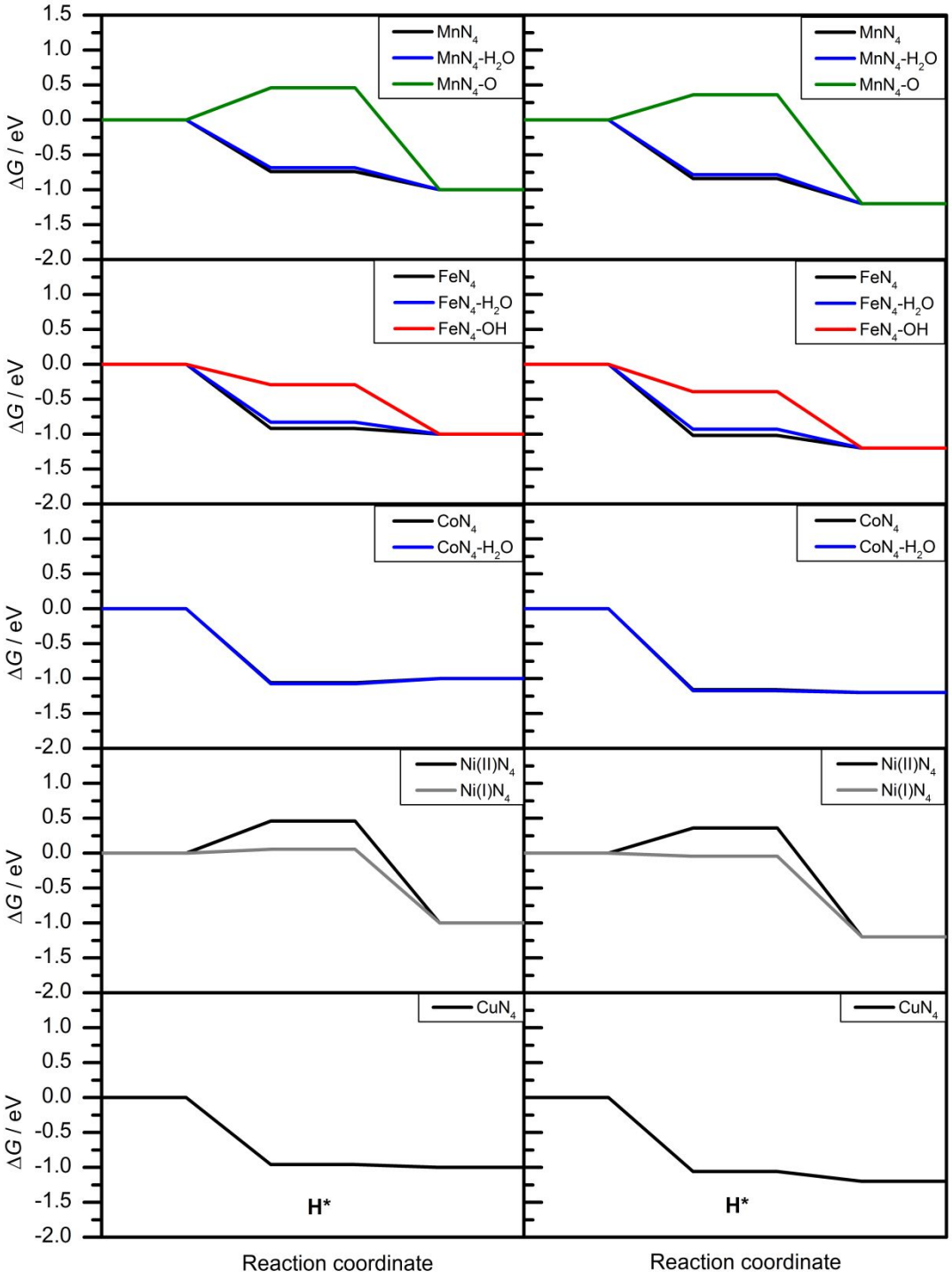

Figure S19. Gibbs free energy profiles of HER over MN_4C_{10} model sites (M = Mn, Fe, Co, Ni and Cu) at pH = 7 and U = −0.5 V (left) and −0.6 V (right) *vs.* RHE, according to the different metal speciation.

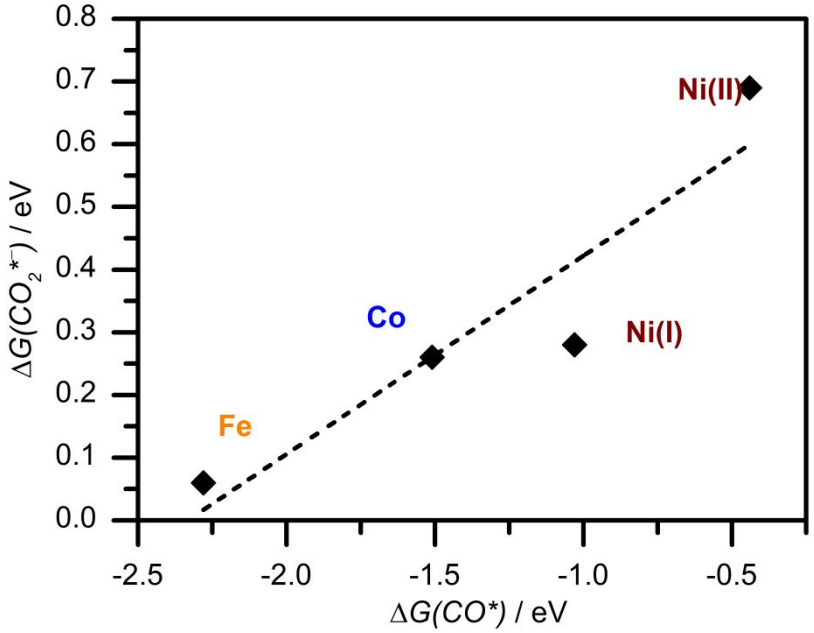

Figure S20. Linear CO_2 binding energy scaling relations for adsorption of CO molecule.

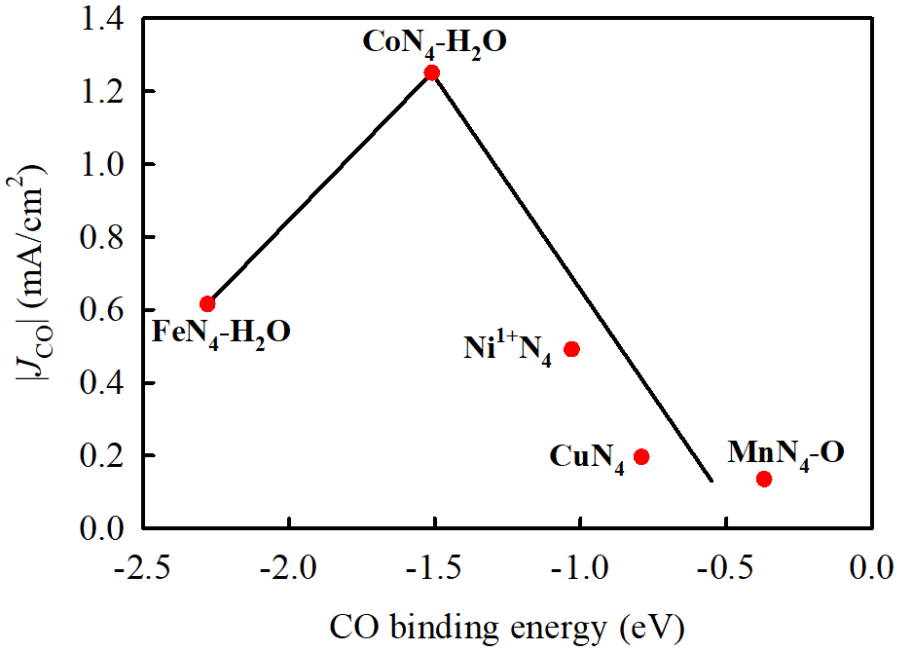

Figure S21. Volcano plot at -0.6 V *vs.* RHE with CO binding energy obtained from DFT simulations as descriptor.

Table S1. Structural parameters obtained from calculated structures.

	MnN_4	FeN_4	CoN_4	NiN_4	CuN_4	ZnN_4
R_{M-N} (Å)	1.91	1.89	1.89	1.88	1.93	1.96
	MnN_4-H_2O	**FeN_4-H_2O**	**CoN_4-H_2O**	**NiN_4-H_2O**	**CuN_4-H_2O**	**ZnN_4-H_2O**
R_{M-N} (Å)	1.91	1.89	1.89			1.97
R_{M-O} (Å)	2.40	2.33	2.31			2.35
	MnN_4-O	**FeN_4-OH**				
R_{M-N} (Å)	1.95	1.90				
R_{M-N} (Å)	1.58	1.81				

Table S2. Elemental composition from XPS analysis, in atomic percentage.

	C	N	O	Zn	M
MnNC	89.5	3.3	7.1	0.13	0.27
FeNC	89.1	6.6	4.1	0.11	0.18
CoNC	91.8	4.3	3.6	0.38	0.24
NiNC	90.5	4.1	5.3	0.32	0.22
CuNC	89.8	3.5	6.6	0.20	0.16
(Zn)NC	91.0	4.5	4.4	0.53	--

Table S3. Relative content (in % of the N_{1s} signal) of various N functionalities in MNC catalysts, derived from the fitting of XPS data.

	N-pyridinic	**N_x-M**	**N-pyrrolic or N-H**	**N-graphitic**	**N-oxide**
MnNC	33.1	15.1	29.2	10.2	12.4
FeNC	31.5	15.7	31.5	10.9	10.4
CoNC	33.4	16.0	30.0	12.6	8.0
NiNC	31.8	16.1	26.7	12.0	13.5
CuNC	34.4	12.8	25.6	13.3	14.0
(Zn)NC	35.6	14.6	26.5	12.5	10.9

Table S4. Surface area and pore volume of MNC catalysts based on N_2 physisorption isotherm analysis, and the electrochemical double layer capacitance (C_{DL}) measured by CV on fresh MNC electrodes.

	BET Surface Area ($m^2 \cdot g^{-1}$)	**Pore Volume ($cm^3 \cdot g^{-1}$)**	**C_{DL} ($\mu F \cdot cm^{-2}$)**
MnNC	311	0.395	545
FeNC	333	0.367	532
CoNC	283	0.219	537
NiNC	223	0.306	580
CuNC	321	0.378	520
(Zn)NC	233	0.2779	572

Table S5. Adsorption energies, magnetisation, and Bader charges for MN_4 systems at 0.0 V *vs.* RHE.

		empty	**CO_2*⁻**	**COOH***	**CO***	**H***
MnN_4	E_{ads} (eV)		1.10	0.19	−0.69	−0.24
	μ_n	2.89	2.89	2.08	1.14	2.12
	q(Mn)(|e⁻|)	1.36	1.36	1.35	1.35	1.33
FeN_4	E_{ads} (eV)		0.89	−0.03	−1.21	−0.42
	μ_n	1.82	0.00	0.81	0.00	0.92
	q(Fe)(|e⁻|)	1.13	1.11	1.09	1.06	1.07
CoN_4	E_{ads} (eV)		0.91	−0.25	−0.36	−0.56
	μ_n	0.82	0.57	0.00	0.00	0.00
	q(Co)(|e⁻|)	0.94	0.95	0.94	0.96	0.93
	E_{ads} (eV)		0.88	0.82	0.17	0.55
$Ni(I)N_4$	μ_n	0.78	0.00	0.38	0.89	0.37
	q(Ni)(|e⁻|)	0.75	0.82	0.93	0.92	0.89
NiN_4	E_{ads} (eV)		1.29	1.22	0.76	0.96
	μ_n	0.00	0.00	0.38	0.00	0.37
	q(Ni)(|e⁻|)	0.86	0.82	0.93	0.88	0.89
CuN_4	E_{ads} (eV)		1.24	1.25	0.41	−0.46
	μ_n	0.54	0.44	0.00	0.54	0.52
	q(Cu)(|e⁻|)	0.95	0.93	0.90	0.96	1.05
ZnN_4	E_{ads} (eV)		3.07	0.64	0.40	0.27
	μ_n	0.00	0.00	0.00	0.00	0.00
	q(Zn)(|e⁻|)	1.14	1.08	1.17	1.16	0.97

Table S6. Adsorption energies, magnetisation, and Bader charges for MN_4-H_2O systems at 0.0 V vs. RHE. Ni, Cu, and Zn systems do not bind oxygen species.

		empty	**CO_2*$^-$**	**COOH***	**CO***	**H***
	E_{ads} (eV)		1.29	0.26	−0.64	−0.19
MnN_4-H_2O	μ_n	2.96	1.58	2.04	1.12	2.11
	q(Mn)(|e$^-$|)	1.42	1.33	1.39	1.32	1.41
	E_{ads} (eV)		0.66	0.09	−1.08	−0.33
FeN_4-H_2O	μ_n	1.83	0.00	0.01	0.00	0.90
	q(Fe)(|e$^-$|)	1.19	1.11	1.19	1.06	1.14
	E_{ads} (eV)		0.96	−0.22	−0.31	−0.57
CoN_4-H_2O	μ_n	0.88	0.61	0.00	0.40	0.00
	q(Co)(|e$^-$|)	1.05	0.96	1.02	1.03	0.99

Table S7. Adsorption energies, magnetisation, and Bader charges for MN_4-OH and MN_4-O systems at 0.0 V *vs.* RHE.

		empty	**CO_2*$^-$**	**COOH***	**CO***	**H***
	E_{ads} (eV)		2.11	1.54	0.83	0.96
MnN_4-O	μ_n	0.46	0.45	2.07	2.03	0.02
	q(Mn)(|e$^-$|)	1.57	1.54	1.46	1.64	1.49
	E_{ads} (eV)		1.55	0.58	−0.43	0.21
FeN_4-OH	μ_n	1.04	0.29	0.86	0.00	0.92
	q(Fe)(|e$^-$|)	1.28	1.26	1.30	1.24	1.22

Table S8. DFT calculated reaction energy ΔG (the free energy of the product minus that of the reactant) at −0.6 V *vs.* RHE for the elementary steps of eCO_2RR to CO. The RDS values correspond to energies corrected by CO and CO_2 gas entropies. All metal cations in +2 oxidation state unless otherwise indicated. FeN_4-H_2O with a high spin state (S = 2) is used.

Reaction Step	DFT calculated reaction energy (ΔG, eV)						
	MnN_4	MnN_4-O	FeN_4-H_2O	CoN_4-H_2O	NiN_4	Ni(I)N_4	CuN_4
A: $CO_2(g) + e^- \rightarrow CO_2{*}^-$	0.49	1.51	0.06	0.36	0.68	0.28	0.64
B: $CO_2{*}^- + H^+ \rightarrow COOH*$	−0.91	−0.57	−0.58	−1.17	−0.07	−0.07	0.01
C: $COOH* + e^- + H^+ \rightarrow CO* + H_2O$	−1.48	−1.31	−1.77	−0.69	−1.06	−1.25	−1.44
D: $CO* \rightarrow CO(g)$	0.63	−0.89	1.02	0.24	−0.83	−0.24	−0.48
RDS	D 0.63	A 1.51	D 1.02	A 0.36	A 0.68	A 0.28	A 0.64